J Solid State Electrochem (2010) 14:1525–1531
DOI 10.1007/s10008-009-0964-5

ORIGINAL PAPER

Study on the capacitance performance of Sn^{4+}-doped V_2O_5

Hong Wang · Zhi-yuan Tang · Jian-xin Li

Received: 22 August 2009 / Revised: 6 October 2009 / Accepted: 19 October 2009 / Published online: 10 November 2009

Abstract Sn^{4+}-doped V_2O_5 cathode materials were prepared by a sol–gel method. The results showed that the modified cathode material was a mixture of V^{4+} and V^{5+}. It was a kind of typical mesopore material with pores of 2–4 nm diameter. Symmetrical curves were obtained by cyclic voltammetry (CV) tests performed at different scanning rates and voltage ranges. In particular, the CV curve showed more obvious rectangle property and better redox properties when the scanning rate was 5 mV s^{-1}. At the current density of 200 mA g^{-1}, the maximum specific energy, specific power, and coulomb efficiency of the material were 27.25 mA hg^{-1}, 494.87 Wkg^{-1}, and 97%, respectively. It was indicated that small amounts of Sn^{4+} doping would improve the surface morphology and electronic conductivity of V_2O_5. The Sn^{4+}-doped V_2O_5 showed good capacitance characteristics.

Keywords V_2O_5 · Cathode material · Electrochemical capacitor · Sn^{4+}-doped

Abbreviations

CV	Cyclic voltammetry
EIS	Electrochemical impedance spectroscopy
XRD	X-ray diffractometer

H. Wang (✉) · J.-x. Li
School of Materials Science and Engineering,
Tianjin Polytechnic University,
Tianjin 300160, China
e-mail: waho7808@163.com

Z.-y. Tang
School of Chemical Engineering and Technology,
Tianjin University,
Tianjin 300072, China

Introduction

Fuel cells and secondary batteries have been used as dynamic power sources of electric vehicles due to their high specific energy. When electric vehicles start and climb, dynamic powers must possess high power density in order to afford the instantaneous high current [1–3]. Therefore, supercapacitors, a new power source, have attracted many scientists' great interests. Hybrid power supplies, composed of high-energy-density fuel cells or secondary batteries and supercapacitors with high power density, are a present trend.

The principle of the double-layer capacitor is that partial ions in the solution were absorbed by carbon electrodes with high specific areas; then, the ions gathered at the solution side of the electrode/electrolyte interface and arranged a certain distance from the electrode, which formed an interfacial film. The charges on the film were equal to those on the electrode surface but had reverse electric properties [4]. This kind of double-layer capacitor has been applied in semiconductor auxiliary power devices, although their specific energy and specific power are relatively low. Through modification, the specific energy of 140 Fg^{-1} can be achieved when the specific surface of carbon aerogel is 2,000 m^2g^{-1} [5]. The research of redox electrochemical capacitors is focused on transition metal oxides of Mn, Ni, and V [6–11]. Both Passerini and Parent proposed the use of vanadium oxide aerogels derived from sol–gel precursors by supercritical drying [12, 13]. These V_2O_5 aerogels can act as high-rate and high-capacity hosts for lithium and shorten the distances of penetration and diffusion, which gave the capacitors high power and densities of energy.

The porous nano-sized V_2O_5 prepared by a sol–gel method and amorphous V_2O_5 prepared by quenching at

950 °C were researched in the literature [14, 15]. V_2O_5 doped with Sn was synthesized by the sol–gel method. After being dried, the 3D reticulated nano-nets were formed due to the collapse of the structure, which could afford the paths for the insertion and emersion of ions in the electrolyte. The energy and power performance of V_2O_5 were improved by doping with SnO_2 because SnO_2 enhanced the catalysis performance of V_2O_5 and enlarged the amount of inserted electrolyte. Jayalakshmi studied the performance of V_2O_5 synchronously doped with SnO_2 and CNT [16].

In this paper, the capacitance performance of V_2O_5 doped with Sn^{4+} was intensively studied with a series of experiments.

Experimental

Preparation of V_2O_5 with Sn^{4+} doping

V_2O_5 (1 g) and SnO_2 (0.0828, 0.124, 0.1656, and 0.207 g, respectively) were mixed and ground fully in agate mortar and then transferred to a flask (material agate ball ratio of about 10:1; milling time 2 h; speed 300 rpm; a one-way rotary). Then, 30% H_2O_2 (100 ml) was adding into the homogenous mixture slowly with stirring, and then acetone (30 ml) was added into the mixture. After stewing for 12 h at room temperature, the mixture turned to red brown gel. The gel was dried for 12 h at 80 °C in an oven. Finally, the cathode material with Sn^{4+} doping was obtained by ball milling in an agate pot.

The chemical reactions were as follows:

$$V_2O_5+2H_2O_2 \rightarrow 2HVO_4+H_2O \quad (1)$$

$$2HVO_4+(n-1)H_2O \rightarrow V_2O_5 \cdot nH_2O+O_2 \quad (2)$$

Preparation of electrodes and assembly of capacitors

The Sn^{4+}-doped V_2O_5 materials were mixed in a blender with acetylene black and polytetrafluoroethylene, with a weight ratio of 85:5:10, and dissolved in ethanol. Then, the three components and ethanol were mixed in a blender. The paste-like mixture was spread uniformly on porous nickel current collectors. After being dried at 120 °C for 12 h and pressed at a pressure of 4 MPa, a mixture with 0.2 mm thickness was formed.

The cells were assembled in a glove box (dried air, moisture content <3 ppm). The FV_3 sulfonating membrane was used as a separator, and the electrolyte used was $MeEt_3NBF_4$(PC).

Electrochemical test of Sn^{4+}-doped V_2O_5 electrode materials

The asymmetry supercapacitors were characterized at room temperature by cyclic voltammetry, electrochemical impedance spectroscopy, and galvanostatic charge/discharge tests. Galvanostatic charge/discharge behavior was performed under the conditions of constant current density of 500 mA g^{-1} in a voltage range of 2.0–0 V with a PCBT-100 equipment. Cyclic voltammetry (CV) and electrochemical impedance spectroscopy (EIS) tests were performed using electrochemical workstation (Gamry Instrument model PCI4-750). EIS was tested at an amplitude of 5 mV in the frequency range of 3×10^5–0.01 Hz. CV was tested in the voltage range of −2–1 V. Sn^{4+}-doped V_2O_5 was the working electrode material, and graphite was both counter electrode and reference electrode material (Table 1).

Characterization of Sn^{4+}-doped V_2O_5 electrode materials

The structure and composite of the products were measured by the X-ray diffractometer (Netherlands PANalytical X' Pert Highscore Co Kα 40 KV, 8°/min, scan range of 5° to 90°). The surface morphology was investigated with the XL30 environmental scanning electron microscope (ESEM; PHLIPS). The samples were attached to an ESEM tube and then sputtered with a layer of Au. The SEM magnification was ×5,000.

Results and discussion

Scanning electron microscopy characterization of Sn^{4+}-doped V_2O_5 electrode materials

Figure 1 displays the ESEM images of V_2O_5 and V_2O_5 doped with Sn. Figure 1a, b shows that the basic V_2O_5 and ball-milled V_2O_5 are submicron-sized and their morphologies are irregular. The particles stacked up in different ways to form submicron-sized particles. From Fig. 1c, it can be seen that the particle sizes of V_2O_5 doped with Sn are obviously smaller than those of V_2O_5 in Fig. 1a, and the doped particles' sizes are distributed evenly. However, the surfaces of the particles are rough because the particles agglomerate seriously. The results show that Sn^{4+} doping could alter the microstructure and the morphology of V_2O_5. Rough surfaces of particles increase specific energy and reduce electrode resistance. Furthermore, the contact areas between electrode material and electrolyte are increased due to the rough surfaces, which is beneficial to achieve the electrochemical active sites, the well

Table 1 Full width at half maximum (FWHM) and *d* of electrode material Sn/V_2O_5

hkl	Oxide	Sn/V_2O_5=0.1		Sn/V_2O_5=0.2	
		d (V_2O_5)/(*A*)	FWHM/(°2Th)	*d* (V_2O_5)/(*A*)	FWHM/(°2Th)
001	V_6O_{13}	13.2635	0.890	12.6009	0.679
104	V_2O_5	3.4425	0.521	3.4731	0.472
152	SnO_2	3.3466	0.479	3.3374	0.336
008	V_2O_5	1.8126	0.617	1.8102	0.172
811	SnO_2	1.7653	0.595	1.7626	0.179

infiltration of the electrolyte, and the improvement of the specific energy.

X-ray diffractometer analysis

Figure 2 shows the X-ray diffractometer (XRD) pattern of synthesized V_2O_5 and V_2O_5 doped with Sn. Figure 2a shows the XRD spectrum (JCPDF card 00-41-1426) of basic V_2O_5 and ball-milled V_2O_5 electrode materials, and Fig. 2c shows the diffraction peak at about 8.14°, which was the characterized peak of V_6O_{13} (JCPDF card 27-1318), and the peaks at 30.9° and 59.1° belonged to V_2O_5 (JCPDF card 52-0794). The peaks at 39.6° and 61.1° were attributed to SnO_2 with increased contents of SnO_2. As strength of the peak increases, the peak width at half height reduces, and the crystallinity and the particle size are augmented. The lattice constants were a=1.43668 nm, b=1.43783 nm, and c=1.43812 nm, respectively, with a molar ratio of Sn/V_2O_5=0.2. After Sn was doped, the lattice of V_2O_5 was distorted, and the electrolyte could penetrate into V_2O_5 more easily, which enhanced the specific energy of the electrode materials.

Study of liquid nitrogen absorption–desorption

Figure 3 shows absorption and desorption isotherms of liquid nitrogen. The absorption isotherm is a typical IV style according to the IUPAC classification. It contains notable hysteresis loops, which indicates that the samples are typical mesopore materials. The absorption and desorption hysteresis loops are H2 style, which indicates that the materials have relatively wide aperture and various hole styles. The specific area of the V_2O_5 xerogel was 121 m^2g^{-1} by Brunauer–Emmett–Teller (BET) test. The total pore volume was 0.2015 cm^3g^{-1}, and the average aperture was 6.6581 nm. The results of the pore distribution calculated by the Barrett–Joyner–Halenda method are shown in Fig. 3a. Most holes are in the range of 2 to 4 nm, and there are also some minipores and macropores.

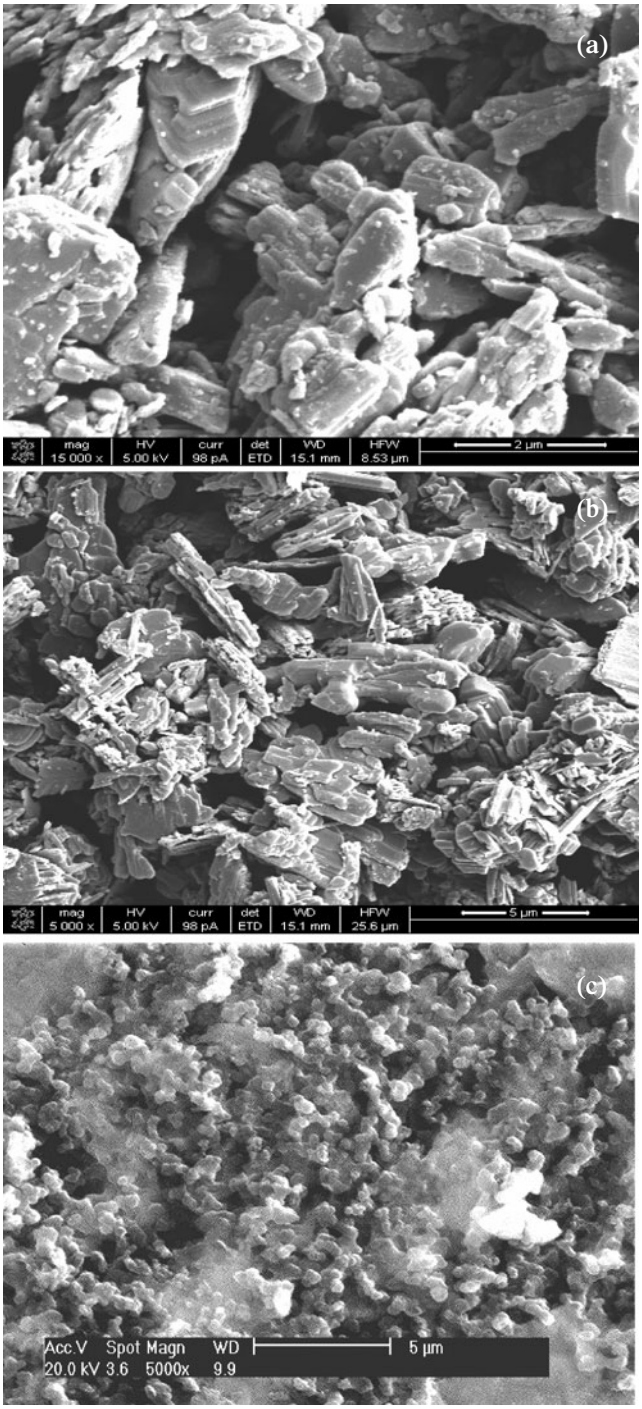

Fig. 1 SEM photograph of **a** basic V_2O_5, **b** ball-milled V_2O_5, and **c** Sn-doped V_2O_5

Specific energy test

Figure 4 shows the relationship between the specific energy and Sn-doping contents. The parabola shape in Fig. 4 illustrates that the specific energy of V_2O_5 xerogel increased at first and then reduced slightly with the increasing contents of Sn. When Sn/V_2O_5=0.2 (mol ratio),

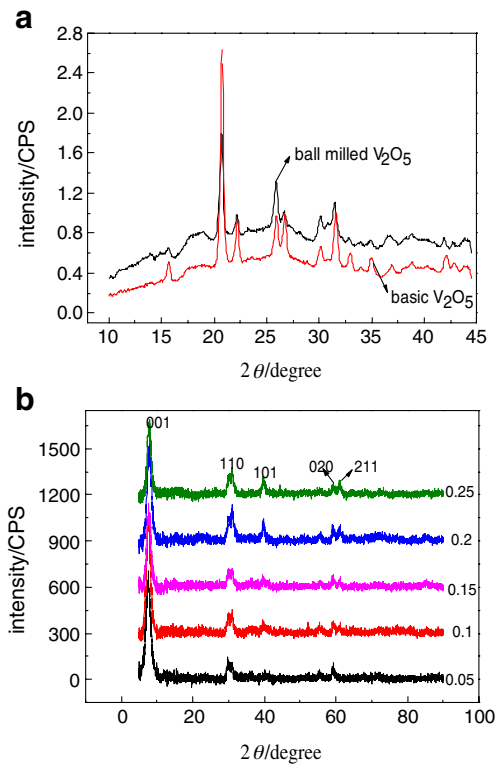

Fig. 2 **a** XRD spectrum of basic V_2O_5 and ball-milled V_2O_5 electrode materials. **b** XRD spectrum of V_2O_5 electrode materials with different Sn^{4+}-doping contents

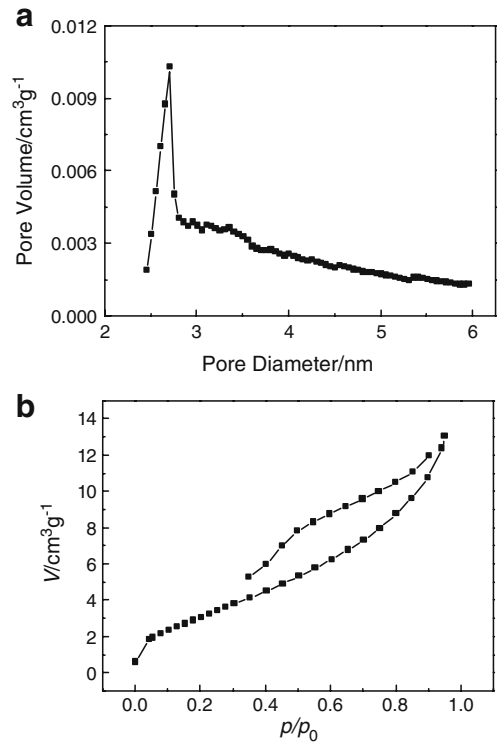

Fig. 3 **a** The adsorption isotherm of the vanadium oxide xerogel. **b** The pore distribution of the vanadium oxide xerogel

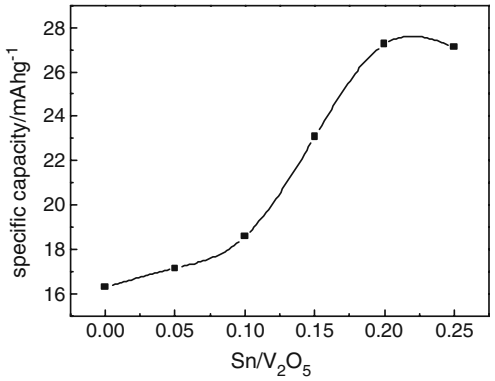

Fig. 4 Specific energy of the samples with different Sn^{4+}-doping contents

the highest specific energy of 27.25 mA hg^{-1} and the highest power of 494.87 Wkg^{-1} were obtained. One possible reason is that V^{4+} and V^{5+} are present in the product V_6O_{13} [16–19]. The other one is that some Sn^{4+} goes into the crystal lattice of V_2O_5 to replace V^{5+}, which leads to more lattice cavities and more energy storage. Additionally, it is helpful to increase the utilization ratio of V_2O_5. In general, energy storage of Sn/V_2O_5 materials is mainly produced by electrochemical reactions on surface. With the increase of Sn-doping contents, the lattice cavities and the quantity of V_2O_5 engaging reaction would increase. Accordingly, the V_2O_5 contents are reduced, which leads to the specific energy being reduced slightly. The result is in accordance with the conclusion of XRD analysis.

Electrochemical impedance spectroscopy

Figures 5 and 6 show impedances of the electrode process. Results indicate that total impedances contains four parts: (a) solution resistance R_1, which is located in the intersection of the hemicycle in high-frequency regions and the real axis in EIS; (b) electrochemical reaction resistance R_2, namely, the diameter of the hemicycle; (c) impedance hemicycle from 10^2 to 10^3 Hz is caused by the

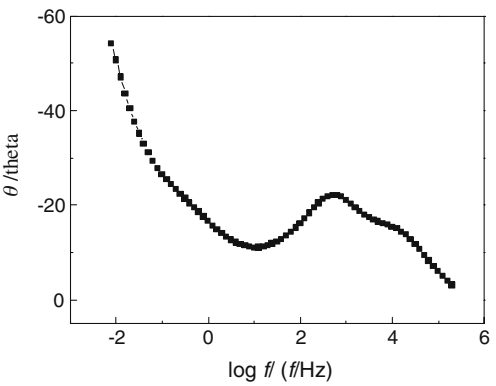

Fig. 5 The impendence frequency spectrum of Sn/V_2O_5

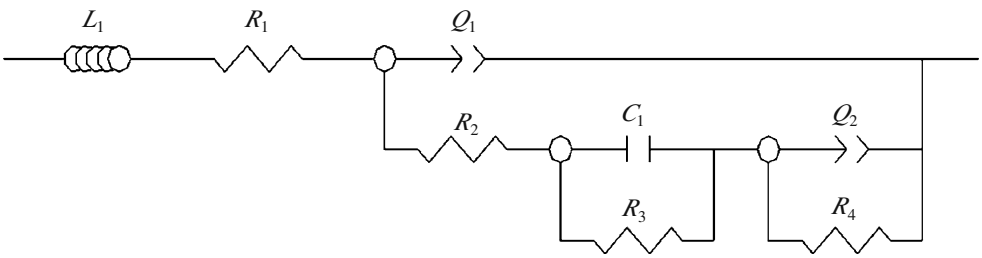

Fig. 6 The equivalent circuit of the V_2O_5 xerogel with Sn doping

adsorption capacitance C_1 and the adsorption resistance R_3; and (d) diffusion capacitance Q_2 and diffusion resistance R_4, which is an upward line under the frequencies of 10^1 Hz. The V_2O_5 xerogel electrode is a porous electrode with various hole styles. From Fig. 5, besides electrochemical reactions, it also includes electrochemical absorption (C_1 and R_3), desorption, and proton diffusion processes (Q_2 and R_4). So it is a very complex electrode process that differs from the ideal capacitor process.

Figure 7 shows the relationship between the impedance spectroscopies of V_2O_5 simulation capacitor and Sn-doped V_2O_5. Nyquist plot contains a hemicycle in the high-frequency regions and a line in the relatively lower-frequency regions, namely, Warburg resistance, generated by ion diffusion. All the points of intersections between the hemicycles in the high-frequency regions and the Z' axis are almost in the same position. This means the intrinsic resistances of capacitors (electrolyte resistance, contact resistance, and electrode resistance) are basically steady. The equivalent series resistances corresponding to the diameters in the high-frequency regions were 23, 20, 15, 11, and 14 Ω, respectively. The result is consistent with (the energy curve in) Fig. 4, in which the intrinsic resistances of the capacitors decreased firstly and then increased with the increasing contents of Sn doping. When the molecular ration of Sn/V_2O_5 is 1:10, the intrinsic resistances of the capacitors were the lowest.

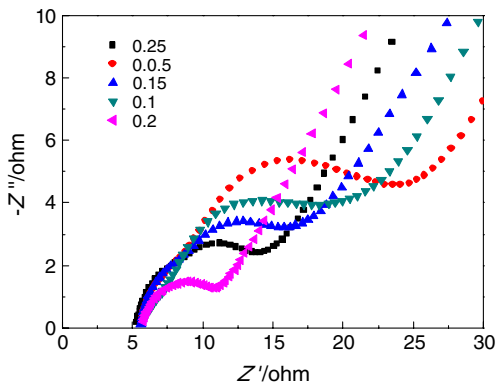

Fig. 7 Impedance spectroscopies of V_2O_5 simulation capacitor with different Sn-doping contents

Leakage current and the self-discharge

Figure 8a showed the relationship between the current and time at a constant voltage. Seen from Fig. 8, current decreased rapidly within several seconds in the initial stage (when the voltage of capacitor reaches the constant voltage). This indicates that the charges on the interface of electrolyte/electrode reached saturation state. In this stage, the current plays a dominant role to maintain discharge current of impurity ions and leakage current of the system. And then, the leakage current of the system becomes dominant and gradually stabilized. The result indicates that the simulation capacitor possessed excellent characteristics of leakage current.

Figure 8b shows the relationships between voltage and time. When the capacitor was charged to different operating voltages, the voltage falls rapidly while being laid aside.

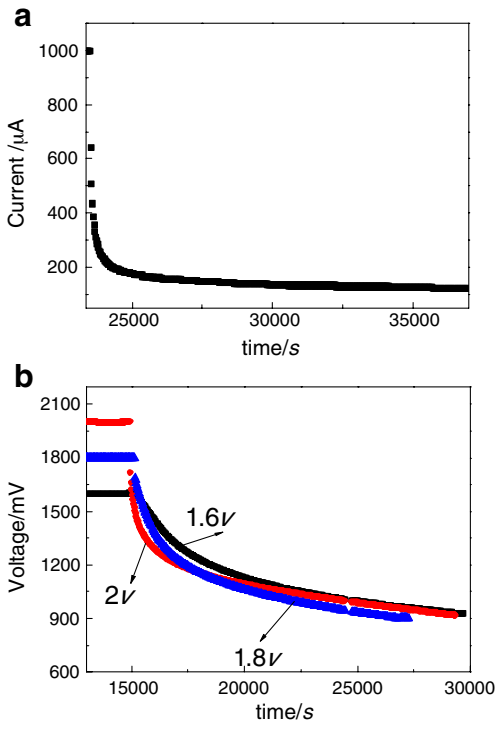

Fig. 8 **a** The 1:10 Sn/V_2O_5 leakage current curve of the simulation capacitor. **b** The 1:10 Sn/V_2O_5 self-discharge curves of the simulation capacitor

The possible reason is that partial voltage is consumed by instant discharge of the equivalent series resistances. Extending time, the drop of voltage becomes mild. A stable voltage of 0.9 V is achieved after 4 h standing, which indicates that self-discharge performance of the electrode is good.

Cyclic voltammetry

Figure 9a showed the CV results with 1 mV s^{-1} scanning rate. From Fig. 9a, a spreading redox peak could be observed at about −1 V, and when scanning voltage exceeds the range of −1.5–0.6 V, a hydrogen evolution peak and an oxygen evolution peak could also be observed. Figure 9b was the CV curve at different scanning rates. The CV curves looked like spindles at the rate of 10 mV s^{-1}. When scanning rates were less than 5 mV s^{-1}, the CV curves exhibited good symmetrical, rectangular characteristics. Inductive currents increased with increasing of scanning rates, and there was a linear relation between the scanning rates and the inductive currents. Namely,

$$I = C\mathrm{d}V/\mathrm{d}t = Ck, \tag{3}$$

where C means the specific capacitance, $\mathrm{d}V/\mathrm{d}t$ is the differential coefficient of the voltage to the time, and k represents the scanning rate. With the increase of scanning rates, the CV curve presented inclining tendency deviating from the rectangular characteristic. The reason is that ions in electrolyte transmitted to the surfaces of electrodes are less than those of consumption due to the increasing currents, which induced the ion quantities on the interface to not meet the discharge requirements of the electrode. Therefore, charges were stored on the electrode, which results in the electron polarization.

The electrochemical potential window is another essential factor in supercapacitors since it directly affects specific power and specific energy. CV curves of the vanadium

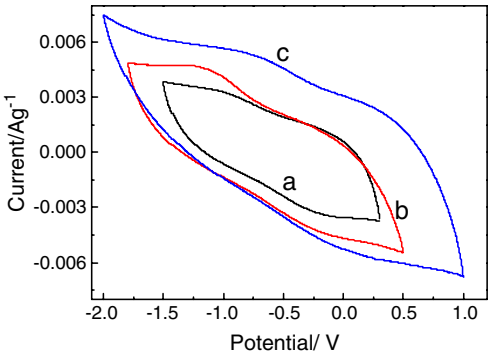

Fig. 10 CV curves of 1:10 Sn/V_2O_5 electrode on various potential limits in 10 mV s^{-1}

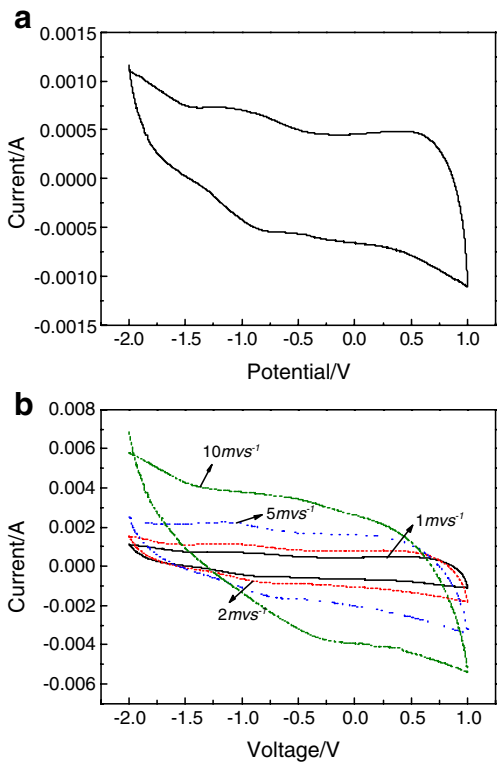

Fig. 9 **a** CV curves of 1:10 Sn/V_2O_5 of simulation capacitor at 1 mV/s. **b** CV curves of 1:10 Sn/V_2O_5 of simulation capacitor at different sweep rates

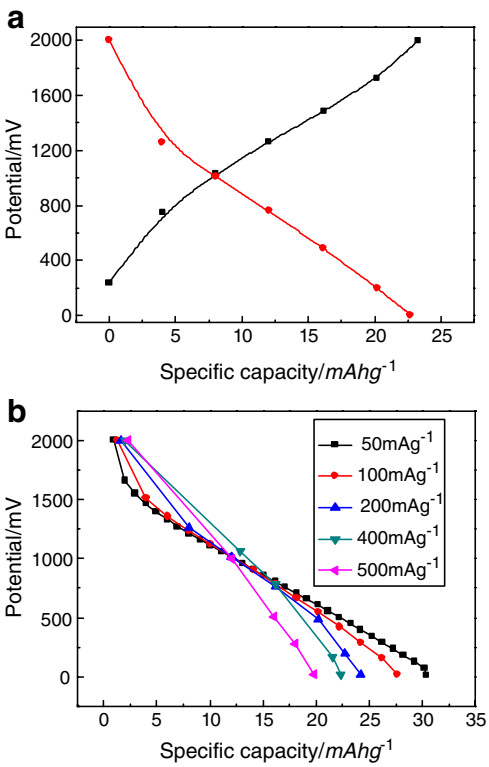

Fig. 11 **a** Charge and discharge curves of the Sn/V_2O_5 simulation capacitor at the current density of 200 mA/g. **b** Discharge curves of the Sn/V_2O_5 simulation capacitor at the current density

oxide electrode with different voltages are shown in Fig. 10; the scanning rate was 10 mV s^{-1}, and $MeEt_3NBF_4$ (1 mol l^{-1}) was used as electrolyte. It can be seen from the figure that all CV curves were symmetrical and approximately rectangular. There were obvious redox peaks, indicating favorable pseudo-capacitance characteristics. There was a distinct hydrogen evolution when the voltage was less than −1.8 V, so the widest electrochemical potential window ranged from −1.8 to 1.0 V. The specific power and specific energy of the electrochemical capacitor increased with the increase of the electrochemical potential window.

Performance testing of capacity

Figure 11a shows the charge–discharge curves of the capacitors at the current density of 200 mA g^{-1}. The specific charge–discharge capacity and coulomb efficiency were 23.262 mA hg^{-1}, 22.727 mA hg^{-1}, and 97%, respectively, which means that the electrode material had relatively high reversibility. Figure 11b shows the discharge curves at different current densities. It was a linear relationship between discharge capacity and voltage. Therefore, the slope of the discharge curve dV/dQ was basically steady, which indicates that the vanadium oxide had electrochemical stability. With the increasing current density, the capacity of the capacitor decreased, and the declined tendency was enlarged with the current density increase. The reason was that, with large current density and short time, the protons and ions were not able to filter into the bulk and stayed at the surface of the electrode, which made the utilization ratio and specific capacity of the active material reduce.

Conclusions

Sn^{4+}-doped vanadium oxide xerogel was prepared with the sol–gel process. Microstructure and surface morphology of V_2O_5 were investigated using BET, XRD, and SEM methods. The doped V_2O_5 was a typical mesopore material with 2–4-nm pores. The results show that the modified cathode material is a mixture of V^{4+} and V^{5+}. Capacity performance and power performance of the doped V_2O_5 were tested by galvanostatic charge/discharge, EIS, and CV methods. Favorable symmetrical curves were obtained at different scanning rates and voltage ranges. The achieved maximum specific energy and specific power are 27.25 mA hg^{-1} and 494.87 Wkg^{-1}, respectively.

Acknowledgment This work was financially supported by the production and research project of Ministry of Education Guangdong Province China (2007A090302006).

References

1. Zhang ZA, Yang BC, Deng MG (2005) J Appl Electrochem 11:58
2. Conway BE (2005) Electrochemical supercapacitors—scientific fundamentals and technological applications. Chemical Industry Press, Beijing, p 45
3. Hirokazu O, Akira Y, Shinsaku M (2006) J Power Sources 158:1510
4. Kudo T, Ikeda Y, Watanabe T (2002) J Solid State Ionics 152:833
5. Sawai K, Ohzuku T (1997) J Electrochem Soc 144:988
6. Chou SL, Cheng F, Chen J (2006) J Power Sources 162:727
7. Wang GX, Zhang BL, Yu ZL (2005) J Solid State Ionics 176:1169
8. Kim IH, Kim JH, Cho BW (2006) J Electrochem Soc 153:A989
9. Cottineau T, Toupin M, Delahaye T (2006) Appl Phys A82:599
10. Leela Mohana Reddy A, Ramaprabhu S (2007) J Phys Chem C 111:7727
11. Xing W, LI L, Yan ZF (2005) Chinese Chem Led 63:1775
12. Zhang F, Passerini S (2001) Electrochem Solid-state Lett 4:A221
13. Parent MJ, Pesserini S, Owens BB (1999) J Electrochem Soc 146:1346
14. Ravinder NR, Ramana GR (2006) J Power Sources 156:700
15. Lee HY, Goodenough JB (1999) J Solid State Chem 148:81
16. Jayalakshmi M, Rao MM, Venugopal N (2007) J Power Sources 166:578
17. Zhou J, Chen W, Xu Q (2002) J of the Chinese Ceramic Society 30:208
18. Wu GM, Xia CS, Du KF (2003) J of TONGJI University 31:1501
19. Chen W, Mai LQ, XU Q (2004) Chem J Chinese Universities 125:904